UC Berkeley
UC Berkeley Previously Published Works

Title

Data-driven airfoil shape optimization framework for enhanced flutter performance

Permalink

https://escholarship.org/uc/item/50d2w6gg

Journal

Physics of Fluids, 36(10)

ISSN

1070-6631

Authors

Jung, Jiyoung

Gu, Grace X

Publication Date

2024-10-01

DOI

10.1063/5.0232055

Jiyoung Jung (정지영) ⓘD ; Grace X. Gu ✉ ⓘD

Check for updates

View
Online

Export
Citation

Articles You May Be Interested In

Prediction and optimization of airfoil aerodynamic performance using deep neural network coupled Bayesian method

Physics of Fluids (November 2022)

Three-dimensional aerodynamic shape optimization with high-order direct discontinuous Galerkin schemes

Physics of Fluids (October 2024)

Flutter instability of rectangle and trapezoid flags in uniform flow

Physics of Fluids (December 2010)

Data-driven airfoil shape optimization framework for enhanced flutter performance ᴇᴘ

View Online   Export Citation   CrossMark

Jiyoung Jung (정지영) 🆔 and Grace X. Gu[a] 🆔

AFFILIATIONS

Department of Mechanical Engineering, University of California, Berkeley, California 94720, USA

Note: This paper is part of the special topic, Fluid-Structure Interaction.
[a]Author to whom correspondence should be addressed: ggu@berkeley.edu

ABSTRACT

This paper presents a machine learning-based airfoil shape optimization framework designed to increase flutter resistance and reduce drag. Using the National Advisory Committee for Aeronautics airfoil as the base design and a Hicks–Henne bump function, we employ multi-objective Bayesian optimization and harmonic balance-based flutter prediction. The optimization process yields a Pareto front revealing trade-off relationships between the flutter speed index and drag coefficient. The optimized airfoils, resembling those of evolved marine animals, outperform the base design in terms of flutter resistance and drag. These results demonstrate the framework's potential to enhance aircraft performance and safety by addressing aeroelastic factors.

As the demand for fast and efficient aircraft structures in the aviation industry increases, aircraft safety is also becoming more prominent. Flutter, a form of flow-induced vibration, is a dynamic instability of an elastic structure in a fluid flow that can lead to catastrophic failure or loss of control. Flutter occurs when the speed of the aircraft exceeds the flutter point due to positive feedback between aerodynamic forces, structural elasticity, and inertial effects, resulting in self-exciting oscillations. Therefore, understanding and mitigating the onset of flutter is a crucial area of research in aerospace engineering. Various methods are applied to the investigation and prediction of flutter.[1–3] As the analytical methods, potential flow-based methods or piston theory-based methods are widely used. Theodorsen's theory, a potential flow-based method, assumes inviscid and incompressible flow using linearized potential flow theory, suitable for low or moderate speeds.[4] Piston theory assumes compressible flow and disturbances normal to the surface, applicable for high-speed conditions.[5] These analytical methods offer computational cost advantages but may not be as accurate under realistic aerodynamic conditions and typically not applicable to complex or 3 D geometries.

On the other hand, computational fluid dynamics (CFD) simulates fluid flow by numerically solving Euler or Navier–Stokes equations. Time-marching CFD-CSD techniques can accurately capture transient, unsteady phenomena, and nonlinear effects by directly simulating and analyzing the interaction between fluid and structure over time.[6–9] The standard procedure for the coupled time-marching approach involves three main steps: a steady simulation with a rigid structure, an unsteady simulation with static structure damping set close to 1, and a dynamic run from the converged deflection. While time domain-based techniques can account for time-transient and complex behaviors, their results are sensitive to time steps, often requiring significant computational cost and storage. Frequency domain-based approaches offer a more efficient alternative by analyzing the system's frequency response characteristics to predict flutter phenomena. These approaches assume periodic solutions, bypassing initial transient states and providing reliable predictions. State variables in these approaches are represented as Fourier series, allowing conversion from a time-domain problem to a frequency-domain problem. The harmonic balance method, widely adopted for flutter prediction, ensures each harmonic component is balanced. This technique has been adapted for CFD analysis to study nonlinear flow in turbomachinery.[10] Additionally, strategies have been improved to determine flutter using the harmonic balance method,[11,12] and a time spectral method-based framework has been proposed as a variational form.[13] The "one-shot" approach, where reduced frequency and reduced velocity are iteratively solved by reducing residuals, has been presented showing reliable solutions, stable convergence, and computational efficiency.[14–18]

The advances in flutter prediction techniques have sparked studies on airfoil shape optimization. However, most studies have adopted adjoint methods for airfoil shape optimization.[19–23] These methods

06 November 2024 18:27:05

rely on gradient calculations of objective variables, enabling efficient exploration of optimal designs, and making them a reasonable choice for airfoil shape optimization, especially given the high computational cost of CFD or flutter analysis. However, as in many other gradient-based optimization methodologies, adjoint methods can be trapped in local optima. From an optimization perspective, a gradient-free optimization framework is needed; at the same time, it must also perform effectively with a relatively small dataset considering the computational cost. Bayesian optimization can be an excellent choice for these types of problems. Bayesian optimization (BO) is a sequential design approach to find a global optimum by repeatedly training a surrogate model, typically Gaussian process regression (GPR), and recommending data points.[24,25] Multi-objective Bayesian optimization (MBO) extends BO to construct a Pareto front for multiple objectives in trade-off relationships using the concepts of hypervolume and appropriate acquisition functions.[26] MBO efficiently explores the global optimum with less data compared to other data-driven optimization methods.[27,28] However, the computational cost of GPR-based BO increases cubically with the number of observations.[29] Therefore, MBO is an optimal choice when the cost of data generation is high, making it difficult to obtain a large amount of data. Given the heavy computation for flutter analysis, MBO is ideal for airfoil shape optimization.

In this study, we present airfoil shape optimization frameworks using MBO to simultaneously enhance flutter resistance and reduce drag as shown in Fig. 1. Our study implements the harmonic balance-based one-shot method for predicting the onset of flutter, balancing accuracy, and computational cost. With the National Advisory Committee for Aeronautics (NACA) 64A010 airfoil as the base design, 10-dimensional parameters for the Hicks–Henne bump function[30] are

selected as inputs to modify the shape of the airfoil, with flutter speed index and drag coefficient chosen as outputs. The trade-off relationship between the flutter speed index and drag coefficient is explored via the Pareto front. The optimized airfoil shapes on the Pareto front are further investigated to identify design characteristics enhancing flutter resistance and reducing drag. This optimization approach has the potential to significantly enhance aircraft structure performance by designing wings that comprehensively consider various aeroelasticity factors, ultimately leading to improved aircraft performance and safety.

A 2D airfoil has been considered to verify the airfoil shape optimization framework. The airfoil possesses two degrees of freedom: pitch and plunge. The airfoil is assumed to be rigid, disregarding any deformation on surfaces. The structural behavior of the airfoil is modeled using two linear springs associated with the pitch and plunge motions, as illustrated in Fig. 2. Damping effects have been neglected in this analysis. Assuming small displacements, the aeroelastic 2D airfoil system is governed by the following linear differential equations:

$$m\ddot{h} + S_\alpha\ddot{\alpha} + K_h h = -L, \tag{1}$$

$$S_\alpha\ddot{h} + I_\alpha\ddot{\alpha} + K_\alpha\alpha = M, \tag{2}$$

$$\text{where } L = q_\infty c C_L, \ M = q_\infty c^2 C_M. \tag{3}$$

Here, α and h are pitching and plunging displacements, respectively. L and M refer to the lift and pitching up moment, m is a mass of the airfoil, S_α is a static moment of inertia about the elastic axis, I_α is the second moment of inertia at the elastic axis, K_α is stiffness of pitching mode, K_h is stiffness of plunging mode, c is chord length, q_∞ is dynamic pressure, and C_L and C_M are lift and moment coefficients,
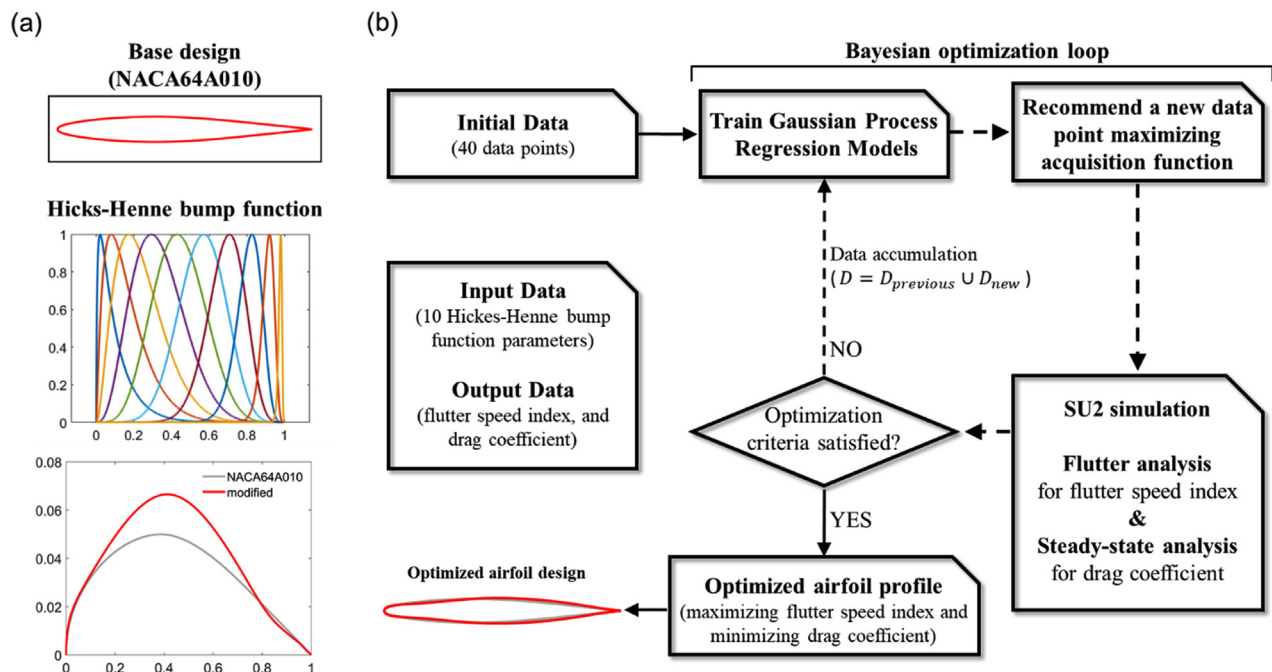
FIG. 1. (a) Shape change methodology for airfoil using the Hicks–Henne bump function, considering NACA64A010 as the base design. (b) Workflow diagram for Bayesian optimization to optimize the shape of airfoil.
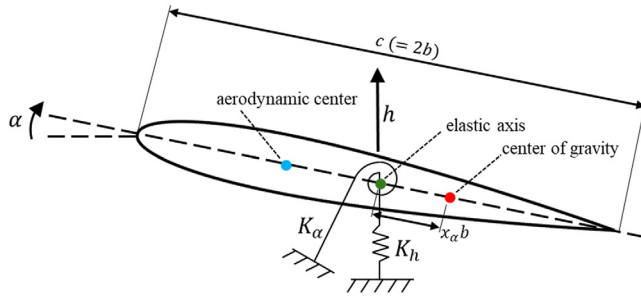
FIG. 2. Schematic of two-dimensional airfoil with two degree of freedom. The structural behavior of the airfoil is modeled using two linear springs associated with the pitch and plunge motions.

respectively. These equations can be rearranged as the matrix form as follows:

$$\boldsymbol{M}\ddot{\boldsymbol{\eta}} + \boldsymbol{K}\boldsymbol{\eta} = \boldsymbol{f}, \quad (4)$$

where $\quad \boldsymbol{M} \equiv \begin{bmatrix} m & S_\alpha \\ S_\alpha & I_\alpha \end{bmatrix}, \quad \boldsymbol{K} \equiv \begin{bmatrix} K_h & 0 \\ 0 & K_\alpha \end{bmatrix},$

$$\boldsymbol{f} \equiv \begin{bmatrix} -L \\ M \end{bmatrix}, \quad \boldsymbol{\eta} \equiv \begin{bmatrix} h \\ \alpha \end{bmatrix}. \quad (5)$$

Here, $\boldsymbol{q}$ is displacement vector, $\boldsymbol{M}$ is a mass matrix, $\boldsymbol{K}$ is stiffness matrix, and $\boldsymbol{f}$ is a force vector. Equation (4) can be further rearranged using the dimensionless variables as follows:

$$\frac{1}{\omega_\alpha^2} \begin{bmatrix} 1 & x_\alpha \\ x_\alpha & r_\alpha^2 \end{bmatrix} \begin{bmatrix} \ddot{h}/b \\ \ddot{\alpha} \end{bmatrix} + \begin{bmatrix} \left(\frac{\omega_h}{\omega_\alpha}\right)^2 & 0 \\ 0 & r_\alpha^2 \end{bmatrix} \begin{bmatrix} h/b \\ \alpha \end{bmatrix} = \frac{V_F^2}{\pi} \begin{bmatrix} -C_l \\ 2C_m \end{bmatrix}, \quad (6)$$

where $\quad r_\alpha^2 \equiv \dfrac{I_\alpha}{mb^2}, \quad \mu \equiv \dfrac{m}{\pi\rho_\infty b^2}, \quad V_F \equiv \dfrac{U_\infty}{\omega_\alpha b \sqrt{\mu}}, \quad x_\alpha \equiv \dfrac{S_\alpha}{mb}.$ (7)

Here, r_α^2 is dimensionless inertia, μ is a mass ratio, V_F is flutter speed index, x_α is dimensionless static unbalance, b is half of the chord length, U_∞ is freestream velocity, ρ_∞ is freestream density, and ω_α and ω_h are uncoupled natural frequencies of pitching and plunging modes, respectively. This approach allows for a simplified yet reasonable representation of aeroelastic behavior, facilitating flutter modeling while maintaining computational efficiency.

We have applied the harmonic balance-based flutter prediction approach to predict the onset of flutter using the open-source software called SU2.[31–33] The technique that we have used is briefly introduced in this section.[18] The frequency domain-based harmonic balance method is computationally efficient compared to the time-marching approaches. The harmonic balance method assumes that flow is periodic, structural vibrations are undamped, and most unsteady aerodynamic problems related to aeroelastic phenomena are periodic in time. In the harmonic balance method, aeroelastic variables can be approximated by a truncated Fourier series, and a vector of conservative variables can be presented with the prescribed number of harmonics (N_H) and given frequency (ω) as follows:

$$\boldsymbol{w}(\boldsymbol{x}, t) = \hat{\boldsymbol{w}}_0 + \sum_{n=1}^{N_H} [\hat{\boldsymbol{w}}_{A,n}(\boldsymbol{x})\cos(\omega n t) + \hat{\boldsymbol{w}}_{B,n}(\boldsymbol{x})\sin(\omega n t)], \quad (8)$$

where $\hat{\boldsymbol{w}}_0$, $\hat{\boldsymbol{w}}_{A,n}$, and $\hat{\boldsymbol{w}}_{B,n}$ are spatial Fourier coefficients of the variable and they can be expressed in time-discrete form as follows:

$$\hat{\boldsymbol{w}} = E\boldsymbol{w}^*, \quad (9)$$

where $\quad \hat{\boldsymbol{w}} = \{\hat{\boldsymbol{w}}_0, \hat{\boldsymbol{w}}_{A,1}, \hat{\boldsymbol{w}}_{B,1}, \ldots, \hat{\boldsymbol{w}}_{A,N_H}, \hat{\boldsymbol{w}}_{B,N_H}\}^T$, $\quad \boldsymbol{w}^* = \{\boldsymbol{w}(t_0), \boldsymbol{w}(t_1), \ldots, \boldsymbol{w}(t_{2N_H})\}^T$, and $t_n = 2n\pi/\omega(2N_H + 1)$. The equilibrium equation of Eq. (6) is transformed into Eq. (10) using the truncated Fourier series and truncated modal shape as follows:

$$\tilde{\omega}^2 \bar{\boldsymbol{D}}^2 \tilde{\boldsymbol{q}}^* + \tilde{\boldsymbol{\Omega}}^2 \tilde{\boldsymbol{q}}^* = V_F^2 \frac{Sb}{2V} \tilde{\boldsymbol{f}}^*. \quad (10)$$

Then, the Eqs. (12) and (13)[18] can be discovered as follows (see supplementary material for complete derivation):

$$\mathcal{L}(\omega, V_F) \equiv \frac{1}{2} \boldsymbol{R}_s^T \boldsymbol{R}_s$$
$$\text{where } \boldsymbol{R}_s \equiv \tilde{\omega}^2 \bar{\boldsymbol{D}}^2 \tilde{\boldsymbol{q}}^* + \tilde{\boldsymbol{\Omega}}^2 \tilde{\boldsymbol{q}}^* - V_F^2 \frac{Sb}{2V} \tilde{\boldsymbol{f}}^*, \quad (11)$$

$$\frac{\partial \mathcal{L}}{\partial \tilde{\omega}} \approx \left(2\tilde{\omega}\bar{\boldsymbol{D}}^2 \boldsymbol{q}^*\right)^T \boldsymbol{R}_s = 0, \quad (12)$$

$$\frac{\partial \mathcal{L}}{\partial V_F} \approx -2V_F \frac{Sb}{2V} \tilde{\boldsymbol{f}}^{*T} \boldsymbol{R}_s = 0, \quad (13)$$

where $\tilde{\omega}$ is normalized frequency, $\tilde{\boldsymbol{q}}^*$ and $\tilde{\boldsymbol{f}}^*$ are dimensionless generalized displacements and external forces at discrete time-instances, $\tilde{\boldsymbol{\Omega}}$ is normalized natural frequency matrix, $V_F \left(\equiv \frac{U_\infty}{\sqrt{\mu} b\omega_1}\right)$ is flutter speed index, S is a reference surface, and V is the volume of the wing. In the one-shot method for flutter prediction using the harmonic balance method, Eqs. (12) and (13) are iteratively solved by proceeding with the following steps. The first step involves conducting harmonic balance-based computational fluid dynamics (CFD) using initial values. Next, perform harmonic balance-based computational structural dynamics (CSD) to update the amplitude and phase of displacements. Following this, update V_F based on Eq. (13). Then, conduct another round of harmonic balance-based CFD. Subsequently, update ω based on Eq. (12). If the solution has converged, the iteration process is terminated. If not, return to conducting CSD with the updated variables and repeat the process until convergence is achieved. For verification of the framework, the bifurcation diagrams of the one-shot harmonic balance method on NACA64A010 are compared to those of previous studies in Fig. S1 (see supplementary material). Our prediction model shows good agreement with the results from previous research.[14,18,34] Detailed explanation of the computational simulations can be found in Methods section.

The airfoil shape optimization is performed following the flow chart in Fig. 1 illustrating the simulation-based MBO framework. For the CFD simulation, a two-dimensional 200×80 quadrilateral elements are generated using Gmsh software[35] for the NACA64A010, which is considered a base design, as shown in Fig. S2 (see supplementary material). For the aeroelastic setup of the airfoil, the elastic axis is placed at $e = 0.2$, static unbalance (x_α) is set to 0.25, dimensionless inertia (r_α^2) is 0.75, mass ratio (μ) is 75, and the natural frequency ratio (ω_h/ω_α) is set to 0.5 as in previous research.[18] Mach number is set to

0.8 and mean of angle of attack is set to zero. Initial values of reduced velocity and frequency for the one-shot harmonic balance method are set at $V_0 = 3.05$ and $\omega/\omega_\alpha = 0.7$, and the initial phase difference is set to $5°$. To predict the onset of flutter, the magnitude of the pitching angle is set to $0.05°$, which should be small enough. The mesh is morphed according to the given 10-dimensional input by employing the Hicks–Henne bump function,[30,36] which is expressed as follows:

$$y^{\text{new}}(x) = y^{\text{base}}(x) + \sum_{i=1}^{n} a_i \sin^t\left(\pi x^{\log_{10}(0.5)/\log_{10}(h_i)}\right), \quad (14)$$

where y^{new} and y^{base} are y-coordinates of the modified and original design, and a_i is the amplitude of the Hicks–Henne bump function. The number of control points (n) is set to 10, Hicks–Henne exponents (t) is five, and x-coordinates of the control points (h_i) along the chord line are defined by "one-minus-cosine" function as follows:

$$h_i = \frac{1}{2}\left[1 - \cos\left(\frac{i\pi}{n+1}\right)\right]. \quad (15)$$

The 10 amplitude values of the Hicks–Henne bump function (a_i) are adopted as design variables. The profiles of the Hicks–Henne bump function and the locations of control points are presented in Fig. S3 (see supplementary material). The amplitude values (a_i) for each control point are limited to the range of $\pm 20\%$ of the y-coordinate of the airfoil profile at the control point, which implies a maximum 20% shape change on the airfoil profile. The airfoil profiles for upper and lower surfaces are symmetrically morphed. As the objectives, the flutter speed index and drag coefficient of the airfoil are considered where the flutter speed index is obtained using the one-shot harmonic balance method, and the drag coefficient is calculated with zero angle of attack. The flutter speed index is related to the stability of the aircraft because a higher flutter speed index implies a later flutter occurrence while a lower drag coefficient means better fuel efficiency. Therefore, an airfoil with a higher flutter speed index and lower drag coefficient would typically be preferred for better performance of aircraft.

MBO is employed for airfoil shape optimization, considering 10-dimensional parameters of the Hicks–Henne bump function as input and the flutter speed index and drag coefficient as output. GPR is adopted as a surrogate model for MBO, which probabilistically predicts objective function for a given input, which enables MBO to explore both high objective regions and high uncertainty regions in a balanced manner using an acquisition function. Detailed procedures for MBO can be found in the Methods section. For initializing MBO, 40 data points are collected using random sampling from a uniform distribution over the input space, as presented in Fig. 3(a). During the data generation, non-converging cases for the one-shot method to calculate the flutter speed index are observed due to an unrealistically wavy airfoil shape as shown in Fig. S4 (see supplementary material). The values of the flutter speed index for those cases are set to zero. MBO is carried out until no further improvement in hypervolume is observed for 15 consecutive iterations, resulting in the process termination after 53 iterations (see Fig. S5 to see MBO iterations vs hypervolume plot in supplementary material). The drag coefficient vs flutter speed index plot after 53 iterations of MBO is shown in Fig. 3(b). From the result, a Pareto front with a high flutter speed index and low drag coefficient is observed. Several optimized designs on the Pareto curve are chosen as shown in Fig. 4(a), and the profiles of those designs are plotted in Fig. 4(b). The values of design parameters and corresponding amplitude values of Hicks–Henne bump functions are summarized in Table S1 (see supplementary material). The flutter speed index and drag coefficient values for the optimized designs are summarized in Table I. One of the optimized designs demonstrates 66.96% enhancements in the flutter speed index at the cost of increasing the drag coefficient 295.05%. Alternatively, another optimized design shows both a 5.15% improvement in the flutter speed index and an 18.09% improvement in the drag coefficient. These results reveal the trade-off relationship between the flutter speed index and drag coefficient on the Pareto front. To emphasize the efficiency of data exploration with MBO, the drag coefficient vs flutter speed index plot using 93 randomly generated inputs is presented in Fig. S6, which is the identical number of data used for MBO (see supplementary material). Comparing Fig. 3(b) and Fig. S6, the result from MBO shows a significantly improved Pareto front compared to that from randomly generated data, which shows the effectiveness of the proposed MBO framework. We note that the obtained Pareto front in Fig. 3(b) does
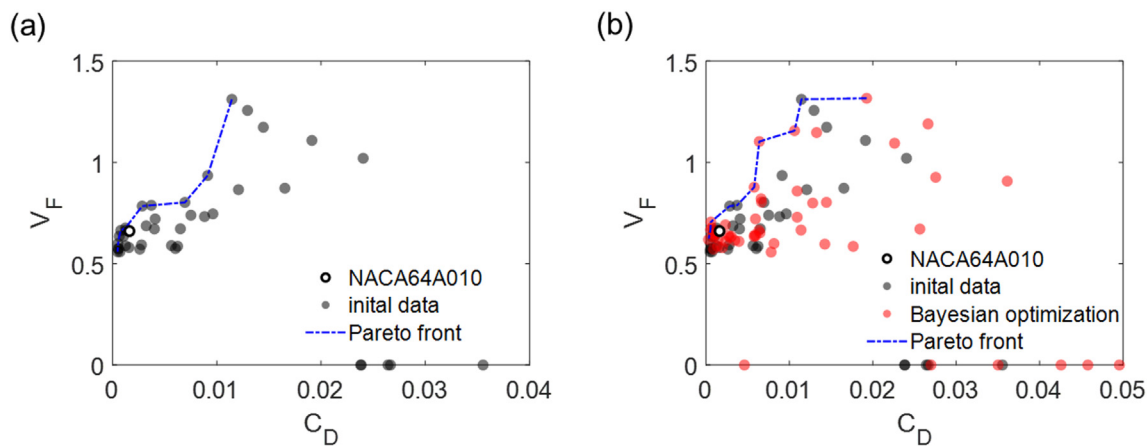

FIG. 3. Drag coefficient (C_D) vs flutter speed index (V_F) plots for (a) 40 initial data with randomly generated inputs and (b) results of MBO after 53 iterations of the optimization loop.
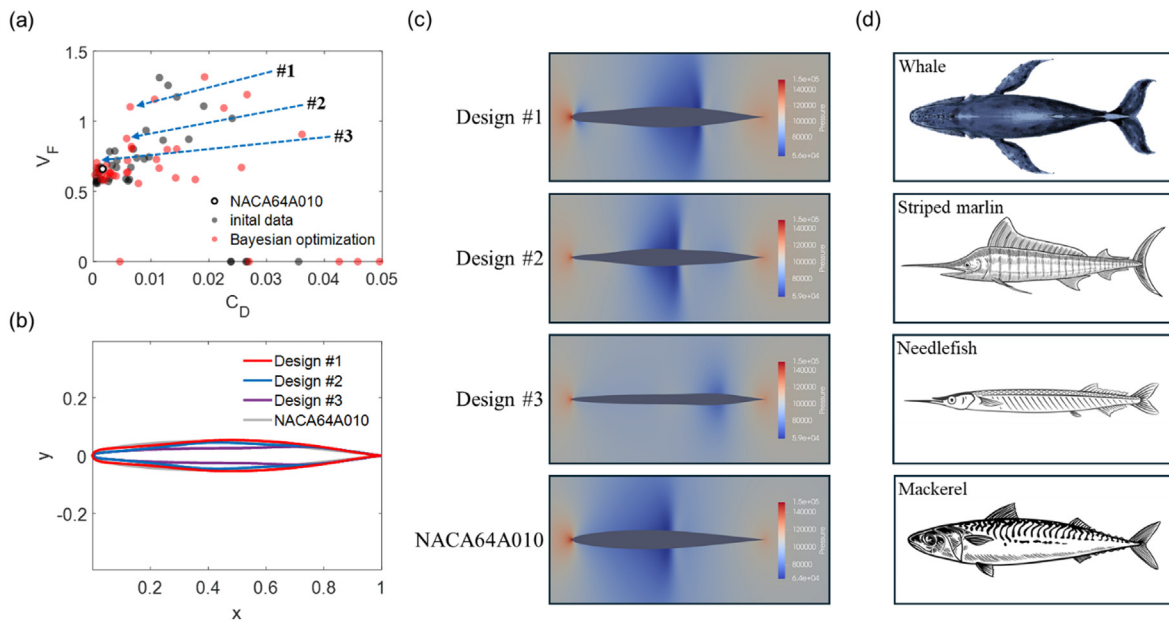
FIG. 4. (a) Optimized designs on Pareto front. (b) Airfoil profiles of optimized designs and NACA64A010, which is base design. (c) Pressure contours for optimized designs and NACA64A010 from harmonic balance method at $t = 0$. (d) The images of marine animals (photo credit: Shutterstock) including the whale, striped marlin, needlefish, and mackerel, which are analogous to the airfoil designs.

not guarantee the global optimum, but it would approach global optimum as MBO further proceeds. As shown in Fig. S7 (see supplementary material), the hypervolume would progressively increase as MBO proceeds, approaching the global optimum. However, considering optimization efficiency and computational cost, the MBO iteration is terminated once the stopping criterion is satisfied.

The pressure contours for the optimized designs and base design are presented in Fig. 4(c), demonstrating different forms of shock waves that characterize the behavior of airfoil. A stronger shock wave is observed in Design #1 compared to Design #3 since Design #1 has more variety in terms of its profile. Interestingly, these optimized designs resemble the top views of marine animals, which have evolved over thousands of years to swim smoothly through fluid, as shown in Fig. 4(d). As the design approaches Design #1, which focuses on stability, it features a gently curved front section and a thickened midsection, reminiscent of the shape of a whale. In contrast, as the design approaches Design #2 and #3, the overall thickness of the airfoil is reduced, resembling the shapes of a striped marlin and a needlefish, which have sharp noses, respectively, while the base design resembles a

mackerel. These similarities highlight potential bioinspired airfoil shapes, even though the flight environments of aircraft and the swimming environments of marine animals are different. Air flow is often assumed to be incompressible in subsonic regime and compressible in transonic and supersonic regime while water is nearly incompressible. Additionally, water is approximately 800 times denser and 50 times more viscous than air. Aircraft are primarily designed to enhance aerodynamic efficiency by reducing drag and increasing lift, while ensuring stability, particularly flutter resistance, under specific operating flight conditions. In contrast, marine animals have evolved streamlined shapes to balance drag reduction with other factors like maneuverability, habitat, and predator avoidance. Nonetheless, it is interesting to note that the optimized airfoil shape presented in this paper shares similarities with the various streamlined shapes observed in marine animals, highlighting potential parallels in their respective approaches to optimizing performance. This highlights the potential discovery of bioinspired airfoil shapes through machine learning-based optimization approaches and the promising application of different airfoil designs depending on different engineering purposes. We believe that this kind of exploration of nature's solutions can inspire and inform innovations in various engineering designs.

While this study has focused on airfoil shape optimization at a fixed Mach number, it is important to note that enhancing flutter performance at one Mach number may affect performance at others. To explore the effect, flutter simulations are performed on the optimized airfoil designs across various Mach numbers, as shown in Fig. S8 (See supplementary material). The results demonstrate that optimization at a specific Mach number does not necessarily lead to improved performance at others. Therefore, to achieve comprehensive flutter resistance across the full operational speed of an aircraft, our optimization

TABLE I. The flutter speed index and drag coefficient values for NACA64A010 and optimized designs. The relative values are calculated by considering NACA64A010 as a reference.

	V_F	C_D	Change in V_F	Change in C_D
NACA64A010	0.6605	0.001616	...	...
Design #1	1.1028	0.006384	66.96%	295.05%
Design #2	0.8772	0.005771	19.65%	65.08%
Design #3	0.7052	0.0005721	5.10%	−18.09%

framework can be extended by incorporating flutter performance at multiple Mach numbers as an objective function.

We have demonstrated a data-driven airfoil shape optimization framework for improved flutter resistance and drag reduction using Bayesian optimization and a harmonic balance-based flutter prediction framework. From the optimization, the Pareto front is obtained revealing the trade-off relationship between the flutter speed index and drag coefficient. The optimized airfoil shape demonstrates superior performance compared to the base design in both flutter resistance and drag reduction. Results show that the optimized airfoil designs could have higher flutter resistance capabilities by sacrificing the drag coefficient or reduced drag coefficient with moderate flutter resistance capabilities along the trade-off relationship. In addition, the optimized designs are reminiscent of the shape of marine animals, which can lead to further investigations on bioinspired airfoil designs. We believe that the methodologies demonstrated in this study can be extended to consider a broader range of aerodynamic characteristics and contribute significantly to the comprehensive optimization of aircraft wings. This advancement holds the promise of making a substantial impact on the aerospace industry, driving innovation, and enhancing the overall performance and safety of future aircraft designs.

More details on the methods for multi-objective Bayesian optimization and computational simulations are discussed below. MBO is employed to optimize the shape of the airfoil, and GPR is chosen as a surrogate model. GPR predicts unknown outputs assuming the observation data ($\boldsymbol{y} = \{y_i | i = 1, \ldots, n\}$) and the prediction ($y^* = f(\boldsymbol{x}^*)$) for unknown input feature ($\boldsymbol{x}^*$) are correlated via multivariate Gaussian distribution as follows:

$$P_{y,y^*} = \begin{bmatrix} \boldsymbol{y} \\ y^* \end{bmatrix} \sim N\left(0, \begin{bmatrix} \boldsymbol{K} & \boldsymbol{k} \\ \boldsymbol{k}^T & k(\boldsymbol{x}^*, \boldsymbol{x}^*) \end{bmatrix}\right), \quad (16)$$

where $\boldsymbol{K} = K_{ij} = k(\boldsymbol{x}_i, \boldsymbol{x}_j)$ is a kernel matrix and $\boldsymbol{k} = k_i = k(\boldsymbol{x}_i, \boldsymbol{x}^*)$ is a kernel vector whose elements are calculated by a kernel function $k(\boldsymbol{x}_i, \boldsymbol{x}_j)$. Here, Matern 5/2 function is adopted as kernel function as follows:

$$k(\boldsymbol{x}_i, \boldsymbol{x}_j) = \sigma_f^2 \left(1 + \frac{\sqrt{5}r}{l} + \frac{5r^2}{3l^2}\right) \exp\left(-\frac{\sqrt{5}r}{l}\right) + \delta_{ij}\sigma_\epsilon^2, \quad (17)$$

$$\text{where } r = \sqrt{(\boldsymbol{x}_i - \boldsymbol{x}_j)^{\mathrm{T}}(\boldsymbol{x}_i - \boldsymbol{x}_j)}. \quad (18)$$

Detailed explanation of the GPR model can be found in Sec. 12 of the supplementary material. To perform multi-objective optimization, MBO adopts the concepts of the Pareto front and hypervolume. The Pareto front represents the set of non-dominated solutions, capturing the tradeoffs between conflicting objectives. Hypervolume measures the region of the objective space dominated by the Pareto front. Based on these concepts, MBO follows a structured sequence of steps to guide the optimization process. First, the GPR model is trained with initial data. Then, the next sample point is recommended where the acquisition function is maximized. Among various acquisition functions, expected hypervolume improvement (EHVI) is adopted as an acquisition function, which is specifically designed for multi-objective optimization, where the goal is to improve the hypervolume dominated by the Pareto front.[37] EHVI effectively balances between exploitation and exploration. Exploitation focuses on refining the current Pareto-optimal solutions while exploration encourages sampling in less-explored regions to potentially better understand the objective space. Flutter simulation is conducted on the recommended sample

point, and newly collected data are added to the previous dataset. The process of training GPR and recommending the next sample are iterated until optimization criteria are satisfied. GPR is implemented by using the Python open-source library "GPy."[38]

For computational simulations, SU2 is implemented, which is open-source software for numerically solving partial differential equations (PDE) in fluid dynamics and aerodynamics problems.[31–33] It includes a built-in coupled fluid–structure interaction solver and a harmonic balance implementation.[39] In this study, 7.5.1. The "Blackbird" version for SU2 is used to conduct CFD simulations. The harmonic balance-based CFD simulation framework in SU2 is integrated with Python scripts for implementing a one-shot method to predict the onset of flutter. Euler solver is adopted for the CFD simulations. To obtain the drag coefficient, another CFD simulation under steady-state conditions is conducted at zero angle of attack. The Mach number is set to 0.8, the freestream temperature is 273.15 K, and the freestream pressure is 101.325 kPa. For simulation, the circular mesh domain is shown in Fig. S2 (see supplementary material), and the diameter of far-field is 100 times the chord length.

SUPPLEMENTARY MATERIAL

See the supplementary material for the nomenclature and further details on the one-shot harmonic balance method and Hicks–Henne bump function. Additionally, bifurcation diagrams for flutter predictions, two-dimensional structured mesh for CFD, non-converging cases for flutter prediction, MBO iterations vs hypervolume plots, and results for randomly generated data are presented, and the optimized design parameters are summarized. Detailed explanation of the GPR model is discussed here.

AUTHOR DECLARATIONS
Conflict of Interest

The authors have no conflicts to disclose.

Author Contributions

Jiyoung Jung: Formal analysis (equal); Investigation (equal); Methodology (equal); Visualization (equal); Writing—original draft (equal). **Grace X. Gu:** Conceptualization (lead); Formal analysis (equal); Methodology (equal); Supervision (lead); Writing—review & editing (equal).

DATA AVAILABILITY

The data that support the findings of this study are available within the article and its supplementary material.

REFERENCES

[1]E. Jonsson, C. Riso, C. A. Lupp, C. E. Cesnik, J. R. Martins, and B. I. Epureanu, "Flutter and post-flutter constraints in aircraft design optimization," Prog. Aerosp. Sci. **109**, 100537 (2019).

[2]T. Abbas, I. Kavrakov, and G. Morgenthal, *Methods for Flutter Stability Analysis of Long-Span Bridges: A Review* (Thomas Telford Ltd, 2017).

[3]E. Antimirova, J. Jung, Z. Zhang, A. Machuca, and G. X. Gu, "Overview of computational methods to predict flutter in aircraft," J. Appl. Mech. **91**, 050801 (2024).

[4]T. Theodorsen, "General theory of aerodynamic instability and the mechanism of flutter Document No. Number," 1979.

[5]W.-W. Zhang, Z.-Y. Ye, C.-A. Zhang, and F. Liu, "Supersonic flutter analysis based on a local piston theory," AIAA J. **47**, 2321 (2009).

[6]N. Fonzi, V. Cavalieri, A. De Gaspari, and S. Ricci, "Extended computational capabilities for high-fidelity fluid–structure simulations," J. Comput. Sci. **62**, 101698 (2022).

[7]J. W. Edwards, R. M. Bennett, W. Whitlow, Jr., and D. A. Seidel, "Time-marching transonic flutter solutions including angle-of-attack effects," J. Aircraft **20**, 899 (1983).

[8]N. Taylor, C. Allen, A. Gaitonde, and D. Jones, "A structure-coupled CFD method for time-marching flutter analysis," Aeronaut. J. **108**, 389 (2004).

[9]I. Jadic, R. So, and M. Mignolet, "Analysis of fluid–structure interactions using a time-marching technique," J. Fluids Struct. **12**, 631 (1998).

[10]K. C. Hall, J. P. Thomas, and W. S. Clark, "Computation of unsteady nonlinear flows in cascades using a harmonic balance technique," AIAA J. **40**, 879 (2002).

[11]J. P. Thomas, E. H. Dowell, and K. C. Hall, "Nonlinear inviscid aerodynamic effects on transonic divergence, flutter, and limit-cycle oscillations," AIAA J. **40**, 638 (2002).

[12]J. Thomas and E. Dowell, "A fixed point iteration approach for harmonic balance based aeroelastic computations," in 2018 AIAA/ASCE/AHS/ASC Structures, Structural Dynamics, and Materials Conference (2018).

[13]S. He, E. Jonson, C. A. Mader, and J. R. Martins, "A coupled Newton–Krylov time spectral solver for flutter prediction," in 2018 AIAA/ASCE/AHS/ASC Structures, Structural Dynamics, and Materials Conference (2018).

[14]H. Li and K. Ekici, "Revisiting the One-shot method for modeling limit cycle oscillations: Extension to two-degree-of-freedom systems," Aerosp. Sci. Technol. **69**, 686 (2017).

[15]H. Li and K. Ekici, "Improved One-shot approach for modeling viscous transonic limit cycle oscillations," AIAA J. **56**, 3138 (2018).

[16]H. Li and K. Ekici, "A novel approach for flutter prediction of pitch–plunge airfoils using an efficient one-shot method," J. Fluids Struct. **82**, 651 (2018).

[17]H. Li and K. Ekici, "Aeroelastic modeling of the AGARD 445.6 wing using the harmonic-balance-based one-shot method," AIAA J. **57**, 4885 (2019).

[18]N. Simiriotis and R. Palacios, "A flutter prediction framework in the open-source SU2 suite," in AIAA Scitech 2022 Forum (2022).

[19]R. Prasad, S. Choi, and M. Patil, "Aerodynamic shape optimization using a time spectral coupled adjoint for nonlinear aeroelastic problems," Aerosp. Sci. Technol. **126**, 107495 (2022).

[20]S. He, E. Jonson, and J. R. Martins, "Wing aerodynamic shape optimization with time spectral limit-cycle oscillation adjoint," in AIAA AVIATION 2022 Forum (2022).

[21]J. Thomas and E. H. Dowell, "Discrete adjoint constrained design optimization approach for unsteady transonic aeroelasticity and buffet," in AIAA Aviation 2020 Forum (2020).

[22]Z. Zhang, P.-C. Chen, S. Yang, Z. Wang, and Q. Wang, "Unsteady aerostructure coupled adjoint method for flutter suppression," AIAA J. **53**, 2121 (2015).

[23]D. Srinath and S. Mittal, "An adjoint method for shape optimization in unsteady viscous flows," J. Comput. Phys. **229**, 1994 (2010).

[24]J. Snoek, H. Larochelle, and R. P. Adams, "Practical Bayesian optimization of machine learning algorithms," in Advances in Neural Information Processing Systems (2012), Vol. 25.

[25]J. R. Gardner, M. J. Kusner, Z. E. Xu, K. Q. Weinberger, and J. P. Cunningham, "Bayesian optimization with inequality constraints," in ICML (2014).

[26]S. Daulton, M. Balandat, and E. Bakshy, "Differentiable expected hypervolume improvement for parallel multi-objective Bayesian optimization," Adv. Neural Inf. Process. Syst. **33**, 9851 (2020).

[27]J. Jung, K. Park, B. Cho, J. Park, and S. Ryu, "Optimization of injection molding process using multi-objective bayesian optimization and constrained generative inverse design networks," J. Intell. Manuf. **34**, 3623 (2023).

[28]K. Park, C. Song, J. Park, and S. Ryu, "Multi-objective Bayesian optimization for the design of nacre-inspired composites: Optimizing and understanding biomimetics through AI," Mater. Horiz. **10**, 4329 (2023).

[29]J. Snoek, O. Rippel, K. Swersky, R. Kiros, N. Satish, N. Sundaram, M. Patwary, M. Prabhat, and R. Adams, *Scalable Bayesian Optimization Using Deep Neural Networks* (PMLR, 2015).

[30]R. M. Hicks and P. A. Henne, "Wing design by numerical optimization," J. Aircraft **15**, 407 (1978).

[31]T. D. Economon, F. Palacios, S. R. Copel, T. W. Lukaczyk, and J. J. Alonso, "SU2: An open-source suite for multiphysics simulation and design," AIAA J. **54**, 828 (2016).

[32]R. Sanchez, R. Palacios, T. D. Economon, H. L. Kline, J. J. Alonso, and F. Palacios, "Towards a fluid-structure interaction solver for problems with large deformations within the open-source SU2 suite," in 57th AIAA/ASCE/AHS/ASC Structures, Structural Dynamics, and Materials Conference (2016).

[33]R. Sanchez, H. Kline, D. Thomas, A. Variyar, M. Righi, T. D. Economon, J. J. Alonso, R. Palacios, G. Dimitriadis, and V. Terrapon, *Assessment of the Fluid-Structure Interaction Capabilities for Aeronautical Applications of the Open-Source Solver SU2* (Crete Island, Greece, 2016).

[34]W. Zhang, B. Wang, Z. Ye, and J. Quan, "Efficient method for limit cycle flutter analysis based on nonlinear aerodynamic reduced-order models," AIAA J. **50**, 1019 (2012).

[35]C. Geuzaine and J. F. Remacle, "Gmsh: A 3-D finite element mesh generator with built-in pre-and post-processing facilities," Numer. Meth. Eng. **79**, 1309 (2009).

[36]G. Yang, A. Da Ronch, J. Drofelnik, and Z.-T. Xie, "Sensitivity assessment of optimal solution in aerodynamic design optimisation using SU2," Aerosp. Sci. Technol. **81**, 362 (2018).

[37]K. Yang, M. Emmerich, A. Deutz, and T. Bäck, "Efficient computation of expected hypervolume improvement using box decomposition algorithms," J. Glob. Optim. **75**, 3 (2019).

[38]GPy, "GPy: A Gaussian process framework in Python," http://github.com/SheffieldML/GPy (since 2012).

[39]A. Rubino, M. Pini, P. Colonna, T. Albring, S. Nimmagadda, T. Economon, and J. Alonso, "Adjoint-based fluid dynamic design optimization in quasi-periodic unsteady flow problems using a harmonic balance method," J. Comput. Phys. **372**, 220 (2018).

06 November 2024 18:27:05